Article:

Lishchuk, A., Lebourg, J., Lishchuk, N. et al. (2026) Strong exciton–plexciton coupling in nickel phthalocyanine thin films on gold. Journal of Applied Physics, 139 (8). 083104. ISSN: 0021-8979

https://doi.org/10.1063/5.0304486

Journal of Applied Physics

RESEARCH ARTICLE | FEBRUARY 23 2026

Strong exciton–plexciton coupling in nickel phthalocyanine thin films on gold

A. Lishchuk ✉; J. Lebourg; N. Lishchuk; A. Campanella; H. Arwin; A. Nabok

J. Appl. Phys. 139, 083104 (2026)
https://doi.org/10.1063/5.0304486

Articles You May Be Interested In

Plexcitonic nose based on an organic semiconductor

Appl. Phys. Lett. (September 2020)

Tunable plexciton dynamics in electrically biased nanojunctions

J. Appl. Phys. (August 2020)

Fano-resonant propagating plexcitons and Rabi-splitting local plexcitons of bilayer borophene in TERS

Appl. Phys. Lett. (June 2023)

AIP Publishing

Journal of
Applied Physics

ARTICLE

pubs.aip.org/aip/jap

Strong exciton–plexciton coupling in nickel phthalocyanine thin films on gold

Cite as: J. Appl. Phys. **139**, 083104 (2026); doi: 10.1063/5.0304486
Submitted: 29 September 2025 · Accepted: 21 December 2025 ·
Published Online: 23 February 2026

A. Lishchuk,[1,a)] J. Lebourg,[2] N. Lishchuk,[3] A. Campanella,[2] H. Arwin,[4] and A. Nabok[5]

AFFILIATIONS

[1] School of Chemical, Materials and Biological Engineering, University of Sheffield, Sir Robert Hadfield Building, Mappin Street, Sheffield, S1 3JD, UK
[2] IUT de Rouen, Rue Lavoisier, 76821 Mont-Saint-Aignan Cedex, France
[3] Tapton School, Darwin Lane, Sheffield S10 5RG, United Kingdom
[4] Materials Optics, Department of Physics, Chemistry and Biology, Linköping University, SE-581 83 Linköping, Sweden
[5] Sheffield Hallam University City Campus, Howard Street, Sheffield S1 1WB, United Kingdom

[a)] **Author to whom correspondence should be addressed:** a.lishchuk@sheffield.ac.uk

ABSTRACT

Strong light–matter coupling is demonstrated in a simple, cavity-free structure consisting of nickel phthalocyanine thin films deposited on gold. Variable-angle spectroscopic ellipsometry, recorded in both conventional and total internal reflection geometries, reveals hybrid exciton–plasmon (plexciton) states with a Rabi splitting up to 0.5 eV. From the ellipsometric data, the transition dipole moment, coupling strength, and Hopfield coefficients are evaluated. Strong coupling is evidenced by abrupt phase shifts in the ellipsometric parameter Δ coinciding with minima in the amplitude parameter Ψ, as well as by topologically distinct ρ-trajectories in the complex reflection plane exhibiting winding numbers of two. Two-dimensional and three-dimensional representations of ρ as a function of the angle of incidence further highlight these signatures of strong coupling. The observed effects depend sensitively on both film thickness and molecular density. The results establish a platform for exploring polaritonic phenomena and suggest potential applications in nanoscale sensing, light-harvesting, and organic optoelectronics.

I. INTRODUCTION

When molecules are confined within an optical cavity, they interact with the resonant cavity photon modes to form exciton–photon polaritons. This phenomenon, known as strong coupling, has been well studied.[1–8] Optical cavities come in many designs and geometries, such as Fabry–Pérot cavities,[9] periodic Bragg reflection structures,[10] microsphere and microdisk resonators,[11] photonic crystal cavities,[12] whispering gallery mode resonators,[13,14] etc. The choice of cavity structure depends on the application and desired optical properties. However, these closed geometries often require complex, multi-step, and time-consuming fabrication processes. To overtake these limitations, open or leaky (also referred to as "open-access" or "planar cavities") optical microcavities have been developed.[15–17] These structures are designed to allow a portion of light to escape, unlike traditional cavities that aim to fully confine light. This controlled leakage serves specific purposes, such as improving sensing capabilities or facilitating light extraction. Recently, cavity-free geometries have emerged as an alternative to both closed and open cavity systems. In such cavity-free geometries, strong coupling arises through delocalized plasmonic modes or simple planar interfaces, rather than from confining light inside a resonant cavity.[16,18]

Based on this concept, we employ a simple cavity-free platform: a thin layer of nickel phthalocyanine (NiPc) deposited on a gold film supported by glass. We investigate its optical response using variable-angle total internal reflection ellipsometry (VA TIRE) and compare it with conventional variable-angle spectroscopic ellipsometry (VASE).

Nickel phthalocyanine [see the chemical structure in supplementary material, Fig. S1-1] is an organic dye that strongly absorbs visible and near-infrared light through exciton formation (bound electron-hole pairs generated when a photon promotes an electron to an excited state while leaving behind a positively charged hole). Its phthalocyanine ring is a large, flat, π-conjugated system in which electrons are delocalized across the entire macrocycle. A central metal ion, such as Ni, mixes its orbitals with those of the ring and slightly alters the molecular symmetry,[19] which shifts the energy levels and transition strengths that determine how the molecule interacts with light. The most prominent feature is the Q band, originating from the lowest-energy π–π^* transition, corresponding to excitation from the ground singlet state (S_0) to the first excited singlet state (S_1). In the solution, the Q band appears near 1.7 eV, but in thin films it typically red shifts to $\sim$1.6 eV due to π–π stacking and excitonic de-localization (Fig. SI-2 in the supplementary material). Molecular aggregation further modifies this band: H-aggregates (face-to-face stacking) usually cause blue shift and broadened absorption, while J-aggregates (partially offset or head-to-tail stacking) lead to red shift and narrowed features.[20–23]

While J-aggregates are popular and effective for studying strong exciton–plasmon coupling, particularly in solid-state cavity-free configurations,[24–26] NiPc derivatives offer several advantages. Unlike J-aggregates, which may exhibit photo-instability,[27] a narrow spectral range,[28] and structural disorder in thin films,[29,30] NiPc offers excellent chemical and thermal stability and easy formation of homogeneous thin films via spin coating. Although NiPc exhibits a broader linewidth than typical J-aggregates, which can limit the maximum observable Rabi splitting, the planar molecular structure of NiPc facilitates anisotropic alignment, thereby enhancing its interaction with surface plasmon modes in ellipsometric and TIRE-based geometries. All these makes NiPc an attractive candidate for the investigation of strong coupling effects.[31]

Thin gold (Au) films deposited on glass serve as a well-known plasmonic platform,[32] supporting surface plasmon resonances across the visible spectral range.[33–35] These resonances originate from the collective oscillation of conduction electrons at the metal–dielectric interface and can be tuned by the excitation wavelength and angle of incidence. By enhancing the local electromagnetic field, surface plasmons enable strong coupling with excitonic transitions in adjacent molecular layers, leading to the formation of hybrid exciton–plasmon states (plexcitons) and making gold a convenient platform for exploring plexciton formation in thin films.[36,37]

Spectroscopic ellipsometry (SE) is a well-established and widely used technique for characterizing thin films,[38] but in plasmonic systems, it often lacks the sensitivity required to detect strong coupling. To address this limitation, we employed total internal reflection ellipsometry (TIRE),[39] which has become increasingly popular for studying plasmon–exciton interactions.[40–44] In this work, both methods were implemented in their variable-angle forms (VASE and VA TIRE), in which the ellipsometric parameters are recorded over a broad range of incidence angles. The VA TIRE configuration, in particular, enhances near-field confinement at the metal–dielectric interface, enabling quantitative evaluation of the Rabi splitting energy, coupling strength, transition dipole moment, and Hopfield coefficients, as well as their dependence on film thickness and molecular density.

In NiPc thin films on gold substrates under cavity-free conditions, phase singularities emerge when the amplitude-related parameter of reflected light (Ψ) approaches zero, causing abrupt changes or undefined values in the phase-related parameter (Δ). Sensitive to resonance conditions, they act as signatures of strong light–matter interactions rather than instrumental artifacts, reflecting interference and coupling phenomena at critical conditions. Their presence provides evidence of plexciton formation, near-field enhancement, and serves as a diagnostic tool for engineering complex photonic systems.[45–47]

II. METHODS

A. Spectroscopic ellipsometry

The rotating compensator spectroscopic ellipsometer M2000-UV by J. A. Woollam Co., Inc. (USA) was employed for all ellipsometric measurements over a photon energy range $E = 1.24{-}3.33$ eV. For VA TIRE measurements, a semi-cylindrical glass prism was used. The prism was in optical contact with the glass side of the metal-coated microscope cover-slip slide via an index-matching fluid (Cargille BK7 glass matching liquid $n_D = 1.5167$, McCrone, UK). Measurements in the TIRE mode were performed in an Teflon$^{\text{TM}}$ cell of 0.2 mL in volume (though it remained empty to enable measurements in ambient air), as shown in Fig. 1.

Ellipsometric measurements were performed using focusing probes (J. A. Woollam Co., Inc., USA), which reduced the spot size, thus minimizing the influence of film non-uniformity from spin coating, allowing reliable measurements on smaller sample areas, and suppressing background reflections (further details are provided in supplementary material, Sec. IC).

Both SE and TIRE mode measurements were conducted first at a fixed angle of incidence (AOI or θ) of 70°, followed by scans over $\theta = 45°{-}80°$ in 0.5° increments. Measurements were

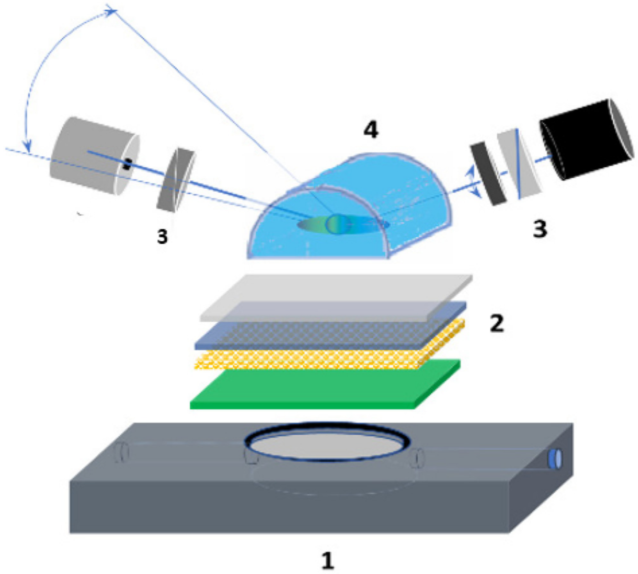

FIG. 1. Schematic diagram shows a VA TIRE setup, with the following labeled components: *1*—Teflon$^{\text{TM}}$ cell, 2—sample, consisting of a microscope glass slide with a thermally evaporated Cr/Au layer and spin-coated NiPc film, *3*—optical components of the ellipsometer (i.e., the polarizer, compensator, and analyzer), *4*—the semi-cylindrical prism.

performed in air. For reproducibility, multiple runs were recorded. Polarization calibration was verified using a standard reference sample (Si wafer with native oxide). The measured ellipsometric parameters (Ψ, Δ) for this reference agreed with tabulated values within $\pm 0.25°$, confirming the accuracy of the calibration. Ellipsometric data were acquired and analyzed using CompleteEASE software (v. 6.67, J. A. Woollam Co., Inc., USA).

B. Deposition of NiPc onto metal surface

Nickel phthalocyanine was dissolved in chloroform to prepare solutions with concentrations c ranging from 1 to 100 mg/mL. Chloroform was selected because it provides high solubility for NiPc and evaporates rapidly during spin coating, which facilitates uniform film formation. Solutions of NiPc is chloroform in various concentrations c (mg/mL) were used in both spin coating and absorption spectroscopy. For deposition, a 20 μl drop of solution was placed onto a rectangular substrate (2.5×2.0 cm), either plain glass or the gold-coated side of a cover-slip glass slide with a thermally evaporated Cr/Au layer, and spread using a spin coater (Ossila Ltd., UK). The spin-coating process lasted 60 s and followed a two-step protocol: the first step was fixed at 800 rpm for 30 s to allow uniform spreading of the droplet, while the second step was varied between 1000 and 2000 rpm for 30 s to control the degree of centrifugal thinning and hence the final film thickness. After spin coating, samples were left to dry in air at room temperature for 10–15 min before measurements.

Using this protocol, a series of NiPc films with thicknesses in the range $d \approx 10-252$ nm were obtained at a fixed solution concentration ($c = 10$ mg/mL). Increasing the second spin speed (up to 2000 rpm) resulted in thinner films due to enhanced solvent removal, whereas lower speeds produced thicker layers. In some cases, the deposited solution volume was increased to 50 μl to ensure complete coverage; potential inhomogeneities were minimized by maintaining the two-step protocol.

This controlled variation of spin-coating parameters enabled systematic investigation of how film thickness and molecular density influence the strength of exciton–plasmon coupling, quantified through the observed Rabi splitting energy.

The illuminated spot in both VASE and VA TIRE measurements is approximately 0.6×2.5 mm (see supplementary material, Sec. IC for details). The NiPc films on both gold and glass substrates demonstrate excellent visual uniformity and appear continuous, smooth, and homogeneous, with no visible aggregates, crystallization features, or defects. Spin-coated metal–phthalocyanine films are reported to form continuous, homogeneous layers with nanometric roughness.[48] Such smooth films are well suited for ellipsometric measurements performed over millimeter-scale illumination areas and fully justify the assumption of optical uniformity within the probed region.

The materials used, together with additional experimental methods (e.g., absorption spectroscopy and determination of the optical parameters and thicknesses of the gold and NiPc layers), are described in the supplementary material Secs. IA, ID, IE, IF, and IG, respectively.

III. RESULTS AND DISCUSSION

Most VASE and VA TIRE measurements are presented and discussed in the supplementary material, allowing the main text to remain focused on key results. Supporting datasets from the supplementary material are cross-referenced alongside the corresponding figures and tables in the main text, without further mention in the text itself.

In this work, the term plasmon–exciton refers broadly to the interaction between plasmonic modes, collective charge oscillations at a metal–dielectric interface, and molecular excitons, i.e., bound electron–hole pairs in the system. This terminology is independent of the coupling regime and applies whether the interaction leads to weak changes or to more pronounced effects.

When the light–matter interaction enters the strong coupling regime, where the coupling strength exceeds the combined dissipative losses of the plasmonic and excitonic components, the system no longer sustains purely plasmonic or excitonic normal modes. Instead, two new hybrid light–matter states emerge (upper and lower polariton branches), separated by the Rabi splitting energy. In this regime, we use the commonly used term plasmon–plexciton to emphasize the formation of mixed states (polaritons) arising from coherent energy exchange between plasmons and excitons on timescales faster than their decay.[2]

Case study note. Before investigating strong coupling phenomena between excitons in NiPc films and metal-supported plasmonic modes, it is important to establish a reliable reference to differentiate true exciton–plexciton interactions from individual optical responses of NiPc and the substrate. For this reason, control measurements were carried out on NiPc films deposited on non-interacting substrates (glass), and clean metal surfaces (gold), in both VASE and VA TIRE modes. To keep clarity in the main text, the corresponding results and discussion are provided in the supplementary material, Secs. IH and II.

A. Types of phase singularities

A phase singularity in ellipsometry refers to a point where the phase-related parameter Δ changes abruptly or becomes undefined; often it is accompanied by a rapid sign change. Such singularities occur when the reflected light amplitude for one polarization component approaches zero, making the phase highly sensitive to small changes in the optical path.

It is essential to distinguish singularities resulting from strong light–matter coupling from those introduced by instrumental or optical artifacts. In the M2000-UV J. A. Woollam Co., Inc. ellipsometer, instrument-related phase flip-overs occur due to internal phase conventions and angle-wrapping logic: the ellipsometric phase Δ is defined modulo 360°, making $-90°$ and 270° mathematically equivalent. The software enforces a continuous representation for plotting and fitting, which can produce apparent discontinuities. Similar artifacts can also occur under conditions of low reflected intensity, such as near the Brewster angle or in the presence of highly absorbing films, where a reduced signal-to-noise ratio introduces instability into Δ readings. Sample misalignment and surface roughness may also generate phase singularities.

Singularities associated with strong coupling are reproducible, angle- and wavelength-dependent, and occur near spectral anticrossings. They are observed in systems with sufficient molecular film thickness and concentration and are accompanied by Rabi splitting features in both Ψ and Δ spectra.

Representative $S = \sin(2\Psi)\sin(\Delta)$ maps, which remove the Δ-wrapping artifacts and reveal the underlying phase evolution, are shown in the supplementary material, Sec. IL.

B. Case study

VASE and VA TIRE measurements of NiPc films were performed under two conditions to separate the effects of optical path length and oscillator density on exciton–plexciton interactions:

(1) NiPc layers with fixed thickness ($d \approx 60$ nm) and varying concentrations ($c = 1 - 100$ mg/mL) and
(2) NiPc layers with fixed concentration ($c = 10$ mg/mL) and varying thicknesses ($d \approx 10-252$ nm) were deposited on the gold substrate. A non-regular NiPc thickness gradient was employed, with finer steps in the $d \approx 42-64$ nm range, where strong exciton–plexciton coupling was expected.

For both conditions, reconstructed dispersion maps derived from the measured $\Psi(E)$ and $\Delta(E)$ spectra are presented for easier visualization of optical mode evolution and identification of strong coupling.

1. Variable concentrations of NiPc

NiPc films were spin-coated onto gold substrates from chloroform solutions with concentrations ranging from 1 to 100 mg/mL. The most representative case, $c = 50$ mg/mL ($d = 63.8 \pm 3.8$ nm), which exhibits clear spectral splitting, is highlighted here. Dispersion maps of Ψ and Δ as functions of photon energy and angle of incidence, measured in both VASE and VA TIRE modes, are summarized in Table I, with the complete dataset provided in supplementary material, Sec. IJ.

1. VASE mode. There are two distinct minima in Ψ around the Q-band, along with sharp phase singularities in Δ. However, the spectral splitting is not angle-dependent and remains nearly constant across all angles of incidence. Such non-dispersive features cannot be assigned to polariton branches but are more consistent with interference effects within the absorbing film. A plausible explanation is Fabry–Pérot-type resonances, which arise from constructive interference between forward- and backward-propagating waves in the NiPc layer. Resulting standing-wave conditions enhance the local field and absorption at specific energies. The angular independence, combined with the vertical film geometry and strong absorption of NiPc, suggests that these features originate from Fabry–Pérot-like resonances that may be influenced by excitonic absorption, rather than from true exciton–plasmon hybridization.

Although such resonances are typically associated with multilayered structures, they could also arise here due to multi-stacking of NiPc aggregates (NiPc is known to self-assemble into columnar stacks via $\pi - \pi$ interactions, particularly at higher concentrations and in thicker films).[49,50] This aggregation can lead to exciton de-localization, Davydov splitting, and alterations in transition dipole orientation. Such excitonic restructuring can shift, broaden, or split optical resonances in a manner that may resemble light–matter coupling.

2. VA TIRE mode. Ψ show clear and well-defined spectral splitting of the resonant mode, strongly indicating the presence of upper and lower polariton branches. The alignment of these features in both Ψ and Δ corresponds to a phase singularity. Δ phase spans is associated with intense mode hybridization in Ψ. These combined features strongly suggest exciton–plasmon hybridization. A quantitative analysis of the Rabi splitting relative to the exciton and plasmon line-widths is presented in the Sec. III C to confirm whether the system satisfies the strong coupling criterion.

2. Variable thickness of NiPc

To isolate the effect of film thickness on the exciton–plexciton interaction, the NiPc concentration was fixed at 10 mg/mL for all samples, while the thickness was varied from ~10 to 252 nm. Under these conditions, changes in d become the dominant factor influencing the optical response.

Results for a $d = 59.6 \pm 4.2$ nm film are shown as a representative example of the behavior observed across the 42–64 nm thickness range. Data for the $d = 10 \pm 2.5$ nm and $d = 252 \pm 13.8$ nm films (presented in supplementary material, Sec. IK) exhibit no clear signatures of strong coupling, such as spectral splitting in Ψ, sharp phase singularities in Δ, or angle-dependent anti-crossing behavior.

1. VASE mode. Ψ and Δ dispersion maps for $d = 59.6 \pm 4.2$ nm are presented in Table II. Narrow, spectrally localized amplitude dips are observed, accompanied by pronounced phase singularities in the corresponding Δ plots. However, these resonances show no angular dispersion. Their spectral position remains constant with θ, distinguishing them from exciton–plexciton resonances. This angular independence, combined with the vertical film geometry and strong absorption of NiPc, suggests that the observed features are Fabry–Pérot-like interference resonances within the absorbing film. These resonances may be influenced by excitonic absorption but do not display the angle-dependent dispersion characteristic of exciton–plasmon polaritons. A similar conclusion was made for fixed-thickness ($d \approx 64$ nm) samples prepared at higher NiPc concentrations ($c = 50$ mg/mL) and measured in VASE mode.

It should be noted that phase singularities are observed at higher photon energies across samples. These are likely instrumental in origin. As mentioned earlier, they can be distinguished from phase singularities associated with strong coupling by the absence of corresponding resonance features in Ψ.

2. VA TIRE mode. A typical VA TIRE dispersion map shown here, represents all samples within the $d \approx 40$–60 nm thickness range (Sec. IK in the supplementary material), which display clear spectral splitting in Ψ and sharp phase singularities in Δ. These features exhibit pronounced angular dispersion, with the energy separation between the upper and lower branches decreasing with θ and forming the anti-crossing pattern characteristic of strong light–matter coupling.

In addition to the upper and lower polariton branches, the ellipsometric spectra also contain an angle-independent excitonic feature at ~1.75 eV (see Tables I–II and SI-8–SI-11 in the supplementary material). This comes from a fraction of NiPc molecules that remain uncoupled from the plasmonic mode. Only the

TABLE I. Comparison of Ψ and Δ dispersion maps for NiPc films on gold ($d = 63.8 \pm 3.8$ nm, $c = 50$ mg/mL) measured in VASE and VA TIRE modes.

Ψ (VASE)	Δ (VASE)
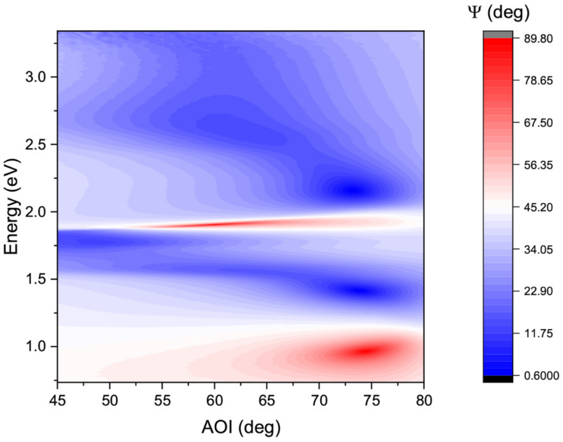	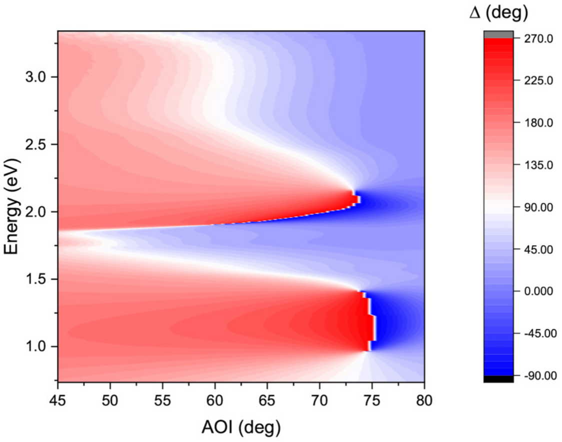
Ψ (VA TIRE)	**Δ (VA TIRE)**
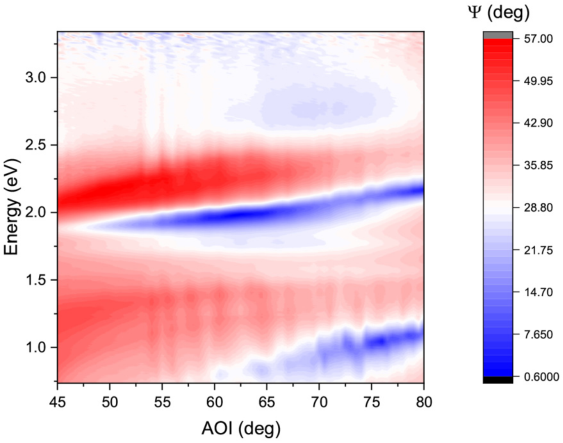	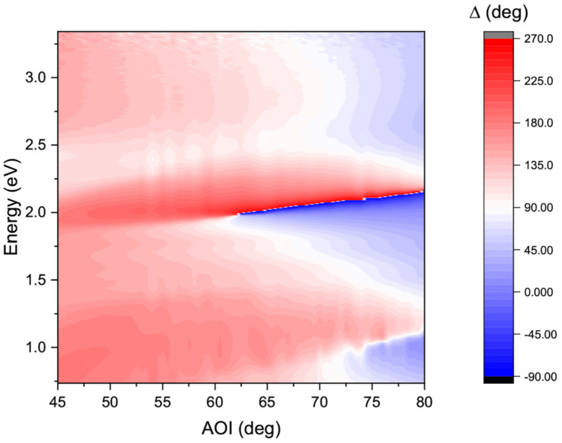

molecules located within the plasmonic mode volume (set primarily by the evanescent field penetration depth of $\delta_p \sim 20–30$ nm) participate efficiently in strong coupling.[3,51] For the thinner films ($d = 42$ nm), approximately $\delta_p/d \approx 25/42 \approx 0.6$, i.e., roughly 60% of the film thickness, lies within the high-field region.

For the thickest films ($d = 64$ nm), this drops to $\delta_p/d \approx 25/64 \approx 0.4$ or about 40%. As the thickness increases, a progressively larger fraction of the molecular layer resides outside the strong-field region and therefore remains uncoupled, giving rise to the angle-independent excitonic line. The coexistence of coupled (dispersive) and uncoupled (angle-independent) excitonic signals is an expected result of finite penetration depth, molecular-orientation distribution, and film-thickness variation.

Compared to VASE measurements, the VA TIRE configuration provides improved sensitivity to angle-dependent spectral features due to the enhanced optical path length and stronger field confinement under total internal reflection. The VA TIRE data strongly suggest that exciton–plasmon hybridization occurs in NiPc films on gold within a well-defined thickness range. A quantitative analysis of Rabi splitting vs linewidths is presented in section III C to determine whether the system fulfills the strong coupling condition.

Comparing the cases of a high-concentration NiPc film ($c = 50$ mg/mL) and a low-concentration film ($c = 10$ mg/mL) of similar thicknesses measured in the VA TIRE configuration, the Ψ and Δ maps show significant difference. In the $c = 50$ mg/mL film, higher molecular density increases the coupling strength but also introduces greater losses from aggregation, disorder, and scattering, leading to broadening the excitonic linewidth and making the avoided crossing appear more diffuse. By contrast, the $c = 10$ mg/mL film, with fewer excitons, has lower coupling strength but also lower damping, producing a cleaner, sharper anti-crossing despite the reduced molecular density.

TABLE II. Comparison of Ψ and Δ dispersion maps for NiPc films on gold ($d = 59.6 \pm 4.2$ nm, $c = 10$ mg/mL) measured in VASE and VA TIRE modes.

Ψ (VASE)	Δ (VASE)
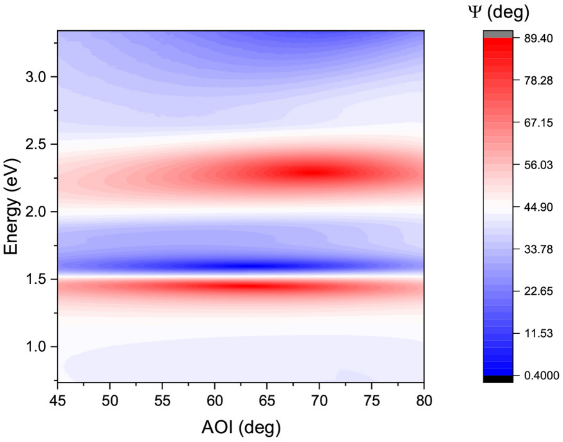	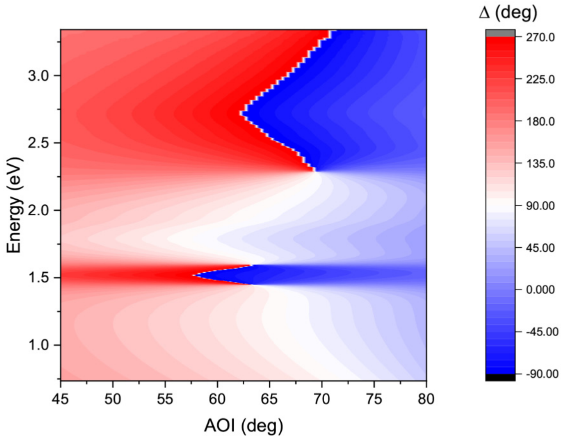
Ψ (VA TIRE)	**Δ (VA TIRE)**
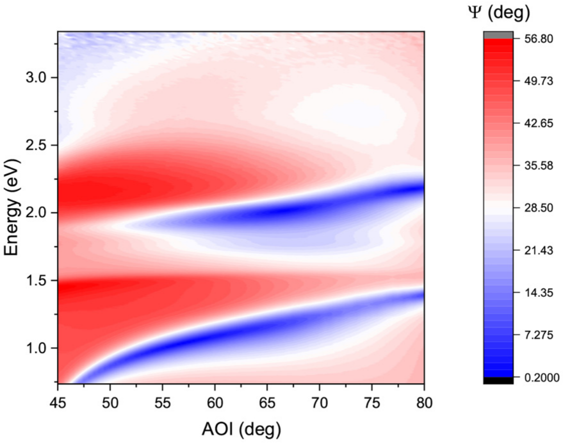	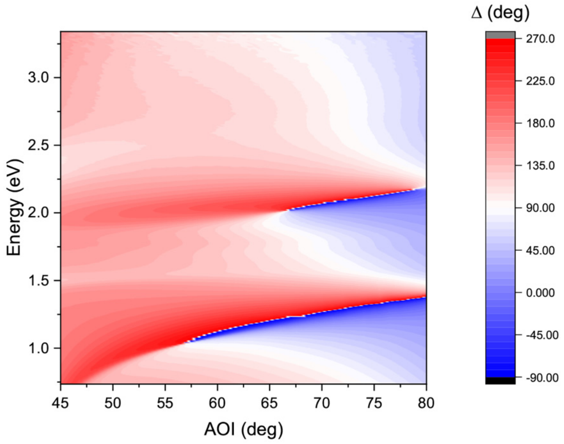

C. Rabi splitting and coupling strength estimation

Despite the simple configuration used, a clear strong coupling, manifested as Rabi splitting and phase singularities, was observed in the ellipsometric Ψ and Δ spectra measured in the VA TIRE mode. To quantify interaction strength, we employed a coupled harmonic oscillator model, commonly used in plasmonic systems.[52]

In our case, the system consists of two oscillators: a molecular excitation in NiPc and a plasmonic mode supported by the metal/organic interface. Their interaction results in the formation of two new energy levels: upper and lower polariton branches:[2,36,52–54]

$$E_\pm(\theta)=\frac{1}{2}\left[(E_0+\alpha(\theta-60^\circ)+E_{ex})\pm\sqrt{(E_0+\alpha(\theta-60^\circ)-E_{ex})^2+4g^2}\right] \qquad (1)$$

Here, $E_0 = E_{pl}(\theta = 60^\circ)$ is the plasmon energy at the central angle used for linearization, E_{ex} is the exciton energy, g is the exciton–plasmon coupling strength, $E_\pm$ correspond to the upper (UPB) and lower (LPB) polariton branches, θ is the angle of incidence, and α is a linear dispersion parameter that accounts for the angular dependence of the uncoupled plasmon mode.

The polariton dispersion relation [Eq. (1)] is obtained by diagonalizing a two-level coupled-oscillator Hamiltonian that describes the interaction between plasmon and exciton modes.[53] The first term, $(E_0 + \alpha(\theta - 60^\circ))$, is a linear approximation of the plasmon resonance energy and represents its shift with angle of incidence. The square-root term describes the characteristic anticrossing, with the coupling strength g defining the Rabi splitting between E_+ and E_-. In this work, the lossless model is used, as it captures the essential physics of mode hybridization and Rabi splitting while keeping the analysis simple. The damped model becomes important when strong absorption or broad resonances dominate and line-width effects must be considered.

Plasmon resonances in planar thin-film structures can shift with θ due to several factors, including phase-matching between light and surface modes, changes in the in-plane wave vector with θ, and variations in the effective optical path length. To avoid recalculating the full angular dispersion for each fit, the plasmon dispersion is approximated as linear about the central angle, $E_{\mathrm{pl}}(\theta) \approx E_0 + \alpha(\theta - 60^\circ)$, with slope α.

At resonance, where $E_0 = E_{\mathrm{ex}}$ and the detuning vanishes, the energy separation between the upper and lower polariton branches defines the Rabi splitting, $\hbar\Omega_R$, which characterizes the coupling strength:

$$\hbar\Omega_R = E_+ - E_- = 2g \tag{2}$$

To confirm that the system is in the strong coupling regime, the Rabi splitting must satisfy the following condition:[2]

$$\hbar\Omega_R > \frac{1}{2}(\gamma_{\mathrm{ex}} + \gamma_0) \tag{3}$$

where γ_{ex} and γ_0 are the linewidths [full width at half-maximum (FWHM)] of the uncoupled exciton and plasmon resonances, respectively. These line-widths reflect the damping or loss rates of the individual modes.

Quality factor Q of each component describes how well-defined a resonance is: higher values indicate narrower resonances, lower damping, and longer coherence lifetimes:

$$Q_{\mathrm{ex}} = \frac{E_{\mathrm{ex}}}{\gamma_{\mathrm{ex}}} \quad \text{and} \quad Q_{\mathrm{pl}} = \frac{E_0}{\gamma_0} \tag{4}$$

The uncoupled plasmon energy E_0 is the energy of the plasmonic mode without strong coupling to molecular excitons. From the TIRE $\Psi(E)$ spectrum of the clean gold substrate, the plasmon dip linewidth was found to be $\gamma_0 = 0.12\,\mathrm{eV}$ at $E_0 = E_{\mathrm{pl}}(\theta = 60^\circ) = 1.35\,\mathrm{eV}$. These values serve as the uncoupled plasmon damping constant γ_0 in the strong coupling condition given in Eq. (3). For consistency, E_0, γ_0, and Q_{pl} were all evaluated at a fixed $\theta = 60^\circ$, selected as a midpoint in the measured range where spectral features are well resolved and fits are most reliable.

Since the film thickness was varied only within a relatively narrow range (including only those samples exhibiting strong coupling), the exciton energy E_{ex} was effectively constant across all samples, with negligible variation. The calculated quality factor was: $Q_{\mathrm{pl}} = 11.25$. Similarly, the exciton energy was fixed at $E_{\mathrm{ex}} = 1.62\,\mathrm{eV}$, based on the position of the Q-band in the UV–vis absorption spectrum of the NiPc film. The line-width of the uncoupled exciton, $\gamma_{\mathrm{ex}} = 0.09\,\mathrm{eV}$, was extracted from the FWHM of the absorption peak. Thus, the exciton quality factor is: $Q_{\mathrm{ex}} = 18.0$. This value remains unchanged across all film thicknesses because it is determined only by the intrinsic properties of the NiPc molecules (i.e., absorption line-width), and is not significantly affected by small changes in film thickness.

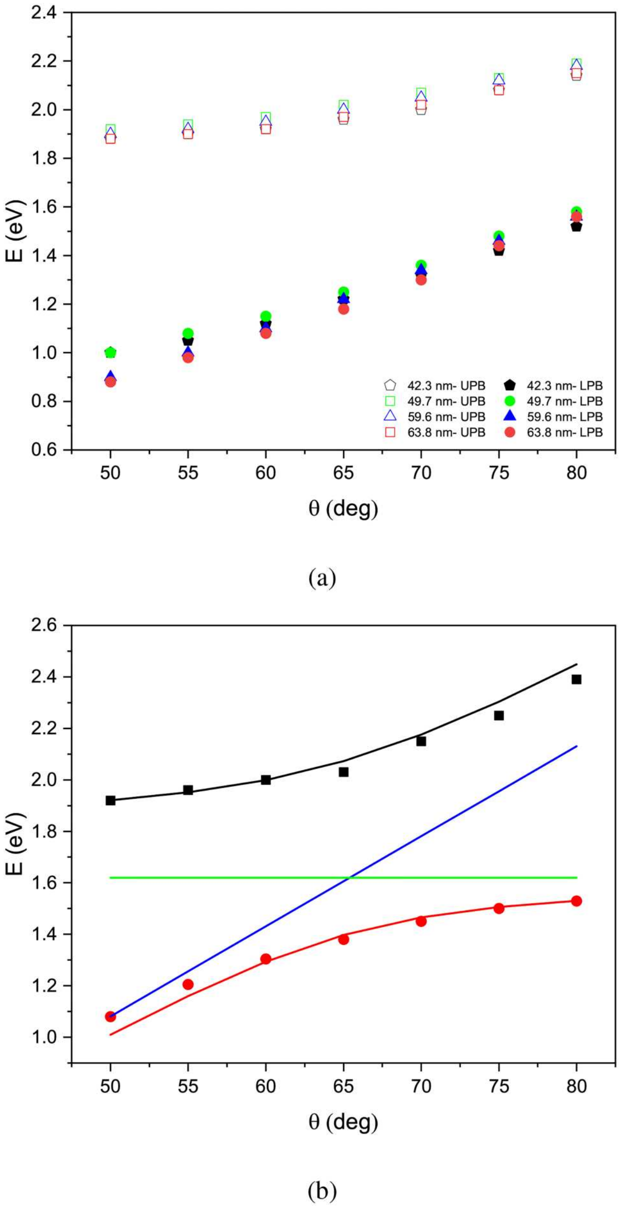

(a)

(b)

FIG. 2. (a) UPB (open symbols) and LPB (filled symbols) extracted from VA TIRE $\Psi(E)$ measurements of NiPc films with varying thickness deposited on gold; (b) UPB and LPB extracted from angle-resolved measurements of a NiPc film on gold ($d = 47.9 \pm 3.6\,\mathrm{nm}$, $c = 10\,\mathrm{mg/mL}$). Symbols represent the experimental LPB (red circles) and UPB (black squares), while lines show the corresponding fitted curves. The green and blue lines denote the energies of free excitons (E_{ex}) and the uncoupled plasmon dispersion ($E_0(\theta)$), respectively.

The decay rate in our system is

$$\frac{\gamma_0 + \gamma_{\mathrm{ex}}}{2} \approx 0.10\,\mathrm{eV},$$

TABLE III. Coupling strength g, Rabi splitting energy $\hbar\Omega_R$, angular dispersion slope α, estimated mode volume V_{mode}, and effective transition dipole moment μ for NiPc films on gold.

d (nm)	g (eV)	$\hbar\Omega_R$ (eV)	α (eV/deg)	V_{mode} (m^3)	μ (D)
42.3 ± 3.1	0.22	0.44	0.022	7.43×10^{-20}	3.90
49.7 ± 3.6	0.18	0.37	0.024	8.73×10^{-20}	4.27
59.6 ± 4.2	0.24	0.47	0.028	1.05×10^{-19}	3.70
63.8 ± 3.8	0.25	0.51	0.051	1.12×10^{-19}	3.53

which is much lower than the measured Rabi splitting (0.37–0.51 eV). Since the coupling energy exceeds the combined losses, this confirms that the system operates well within the strong coupling regime. Despite the relatively modest Q-factors, the large Rabi splitting and narrow excitonic line-width enable polariton formation, demonstrating efficient light-matter hybridization under the given experimental conditions.

Ellipsometric dispersion data for NiPc films with thicknesses ranging from ∼42 to 64 nm ($c = 10$ mg/mL) on gold substrates exhibit clear mode splitting and anti-crossing behavior (Tables SI-8–SI-11 in the supplementary material). The UPB and LPB were extracted from the Ψ spectra over $\theta = 50-80^\circ$, with the complete dataset shown in Fig. 2(a). The $d = 47.9 \pm 3.6$ nm film is presented as an example since it displays the characteristic spectral features typical for this thicknesses, in contrast to thinner ($d \approx 10$ nm) and thicker ($d \approx 252$ nm) films, which exhibit no signatures of strong coupling (Tables SI-7 and SI-12 in the supplementary material). The fit of the experimental data to Eq. (1) is shown in Fig. 2(b).

In Table III, the coupling strength g, Rabi splitting $\hbar\Omega_R$, and the angular dispersion slope α of the plasmon mode were extracted from VA TIRE Ψ data using a coupled oscillator model. For each film thickness, the experimental data were fitted by solving the real part of Eq. (1), and the optimal value of g was determined by minimizing the squared deviation between the experimental and fitted data. Although the UPB and LPB are real in an ideal lossless model, in practice the solutions of Eq. (1) become complex because of damping. We compare only the real part, which gives the mode energies, while the imaginary part corresponds to linewidths and is not fitted here. The Rabi splitting was then calculated using Eq. (2).

The observed Rabi splitting energies are well above the typical threshold for entering the strong coupling regime, and are comparable to or even exceed previously reported values for organic systems.[55,56]

The coupling strength and Rabi splitting values show no clear correlation with film thickness (Table III). In thin films, even small variations can strongly influence optical modes through interference effects. While spin-coating generally provides good reproducibility, factors such as edge effects, film inhomogeneity, and local substrate defects can introduce variability in thickness. Ellipsometric measurements, performed with focusing probes yielding a maximum spot size of ∼0.56 mm through the prism, provide high local precision. In contrast, thickness measurements from the Bruker 3D optical interferometer (white-light interferometry) are limited by the instrument's vertical resolution of ∼1 nm and lateral resolution of ∼0.5−1 μm, where lateral resolution refers to the smallest resolvable surface features in the x–y plane, distinct from the total field of view. For semi-transparent thin films below 100 nm, multiple reflections, refractive index assumptions, and local roughness effects can further degrade accuracy. These combined uncertainties often produce overlapping thickness values for nominally distinct samples and overlapping Rabi splitting energies, complicating a clear correlation between thickness and coupling strength.

D. Resonant angle and Hopfield coefficients

The excitonic and photonic composition of the LPB and UPB varies with θ because the plasmon energy shifts with angle, whereas the exciton energy remains fixed. At small θ, the plasmon lies below the exciton energy (negative detuning), so the LPB is primarily excitonic while the UPB is primarily photonic. As θ increases, the plasmon energy rises above the exciton energy,[57,58] leading to positive detuning and reversing the dominant character of the two branches. At zero detuning, when the plasmon and exciton energies coincide, the system reaches maximum hybridization: the LPB and UPB contain equal excitonic and photonic fractions, producing the clear anti-crossing in the dispersion curves. The relative contributions of the uncoupled exciton and plasmon modes to the polariton states are described by the Hopfield coefficients. They quantify the angle-dependent mixing of exciton and photon states. Hopfield coefficients are calculated from the coupled harmonic oscillator model as follows:[59]

$$\left|C_{\text{ex}}^{\text{LPB}}(\theta)\right|^2 = \frac{1}{2}\left(1 - \frac{\delta(\theta)}{\Omega(\theta)}\right), \tag{5}$$

$$\left|C_{\text{ex}}^{\text{UPB}}(\theta)\right|^2 = \frac{1}{2}\left(1 + \frac{\delta(\theta)}{\Omega(\theta)}\right) \tag{6}$$

where $\delta(\theta) = E_0(\theta) - E_{\text{ex}}$ is the detuning, and

$$\Omega(\theta) = \sqrt{\delta(\theta)^2 + 4g^2} \tag{7}$$

is the generalized Rabi frequency. The corresponding photonic fractions are given by $|C_{\text{ph}}|^2 = 1 - |C_{\text{ex}}|^2$.

Figure 3(a) presents the calculated exciton fractions of the LPB and UPB as a function of θ for NiPc films of varying thicknesses deposited on gold, evaluated using Eqs. (5) and (6).

Thickness-dependent Hopfield coefficients reveal a clear correlation between the photonic and excitonic fractions within the polariton branches. For thinner NiPc films (e.g., $d = 42.3 \pm 3.1$ nm), the LPB is predominantly photonic, with Hopfield coefficient ∼0.9 at lower θ, indicating minimal excitonic contribution. As the film thickness increases, the excitonic fraction in the LPB rises, while the photon fraction in the UPB correspondingly increases, indicative of enhanced exciton–plexciton coupling.

The angle of maximum mixing, defined as the point where the LPB and UPB Hopfield coefficients both approach 0.5, decreases with increasing NiPc film thickness [Fig. 3(b)]. For thinner films, this crossing occurs near 72°, whereas for thicker

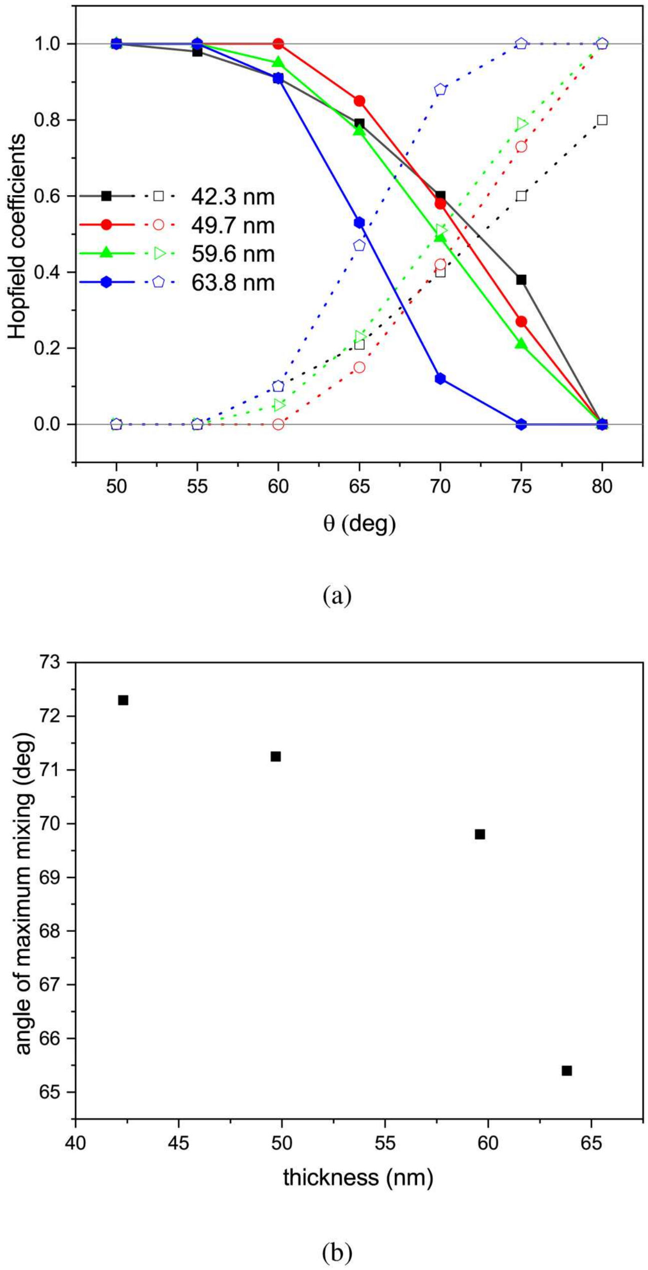

(a)

(b)

FIG. 3. (a) Calculated Hopfield coefficients for NiPc films of varying thickness on gold. Solid and dotted lines correspond to the LPB and UPB, respectively; (b) Dependence of the angle of maximum mixing (Hopfield crossing point) on the thickness of NiPc films deposited on gold at a fixed $c = 10$ mg/mL.

films (e.g., $d = 63.8 \pm 3.8$ nm), it shifts to around 65°. This shift reflects the enhanced overlap between the plasmonic field and the excitonic medium in thicker films, which modifies the phase-matching conditions and enables strong hybridization at lower angles.

Although the molecular density was kept constant across all samples ($c = 10$ mg/mL), increasing the film thickness enhances the exciton–plasmon interaction in two ways. First, a thicker film increases the number of excitonic dipoles participating in the coupling, since the interaction strength scales approximately as $g \propto \sqrt{N}$, where N is the number of excitons coupled to the plasmonic mode.[2] Second, the larger thickness improves the spatial overlap between the confined plasmonic field and the excitonic medium, thereby modifying the phase-matching conditions and shifting the angle at which maximal hybridization occurs to lower θ. Thus, variations in film thickness, even at constant molecular concentration, provide direct control over the detuning, exciton–photon mixing ratio, and overall coupling strength.

The flattening of Hopfield curves at higher θ for thicker films may indicate a saturation of the excitonic contribution, potentially influenced by inhomogeneous broadening or dephasing at large incidence angles.

E. NiPc layer molecular density, mode volume, and transition dipole moment

From the measured Rabi splitting values for NiPc films with thicknesses in the range $d \approx 42-64$ nm on gold (prepared from a $c = 10$ mg/mL solution), key physical parameters[2] (e.g., molecular density, transition dipole moment, and optical mode volume) relevant to the strong coupling regime were estimated.

The molecular density (N) represents the number of optically active molecules per unit volume. The molecular density N was calculated using:

$$N = \frac{\rho N_A}{M} \tag{8}$$

where the solid-state density of NiPc is $\rho = 2\,\mathrm{g/cm^3}$ was adopted as a practical approximation (since the Rabi splitting scales with $\sqrt{N}$, moderate deviations from literature values[22] ($\rho \approx 1.6\,\mathrm{g/cm^3}$) introduce only minor errors in the estimated coupling strength), the molar mass $M = 1148.1$ g/mol,[60] and $N_A = 6.022 \times 10^{23}\ \mathrm{mol^{-1}}$ is Avogadro's number. The resulting value was approximately $N \approx 1.15 \times 10^{27}\ \mathrm{m^{-3}}$.

The optical mode volume (V_{mode}) defines how "tightly" the electromagnetic field is confined in space; smaller mode volumes increase the local field strength for a given number of excitons, thereby enhancing light–matter coupling and leading to larger Rabi splittings in systems such as NiPc–plasmon interfaces. The mode volume was estimated as:

$$V_{\mathrm{mode}} = A \cdot d, \quad \text{with } A \approx \left(\frac{\lambda}{n}\right)^2 \tag{9}$$

where A represents the effective mode area of the confined optical field, $\lambda = 838$ nm is the wavelength of coupled optical mode, $n \approx 2$ is the effective refractive index (although the precise value depends on film thickness and optical anisotropy), and d is the NiPc film thickness.

The transition dipole moment (μ) of the NiPc exciton is a key parameter because it directly determines how strongly light interacts with the material. The strength of this interaction is reflected in the Rabi splitting energy ($\hbar\Omega_R$), which increases with both the magnitude of μ and the number of excitons that couple coherently to the optical mode, while decreasing with the mode volume. A larger μ means stronger coupling and a clearer separation of the upper and lower polariton branches. In NiPc thin films, the flat, planar molecular structure naturally aligns the dipoles with the confined plasmonic field, which may enhance the interaction strength and making it easier to observe the distinct features of strong coupling in the ellipsometric spectra.

The transition dipole moment μ was calculated from the expression:[61]

$$\mu = \sqrt{\frac{(\hbar\Omega_R)^2 \cdot \varepsilon_0 \varepsilon_m V_{\text{mode}}}{N}} \tag{10}$$

where $\hbar\Omega_R$ is the Rabi splitting (in eV), V_{mode} is the mode volume (in m^3), N is the molecular density (in m^{-3}). The vacuum permittivity is $\varepsilon_0 = 8.85 \times 10^{-12}$ F/m, and $\varepsilon_m = 2.5$ is the background dielectric constant. This value reflects the effective permittivity of the local electromagnetic environment near the NiPc–gold interface, considering both the organic layer ($n \approx 2$) and its surroundings (e.g., air and substrate). The choice of $\varepsilon_m = 2.5$ is consistent with values reported for similar plasmon–exciton systems.[37,43,62]

The calculated dipole moments were converted to Debye (D), and together with the mode volumes, are summarized in Table III for NiPc films with thicknesses ranging from ca. 42 to 64 nm.

Adjustment of μ, N, and V_{mode} enhances the light–matter interaction, resulting in the clear formation of upper and lower polariton branches in NiPc/plasmon interfaces.

F. ρ trajectory

In addition to the conventional representation of ellipsometric results in $\Psi(E)$ and $\Delta(E)$ (or the corresponding reconstructed dispersion maps), the optical response of NiPc films was further analyzed using the complex reflection ratio:

$$\rho = \tan\Psi \cdot e^{i\Delta} \tag{11}$$

Ψ and Δ both originate from the same underlying complex reflection coefficients, describing the amplitude ratio Ψ and phase difference Δ separately.[63] Representing them jointly as ρ, combines this information into a single parameter and provides a clear visualization of the spectral signatures of strong coupling.[47,64,65] In the strong-coupling regime, the phase of ρ exhibits characteristic winding and multi-loop behavior associated with coherent energy exchange between excitons and plasmons. This highlights features that may be difficult to identify in conventional Ψ and Δ maps alone.

The trajectory of ρ in the complex plane is characterized by its winding number. It represents the total number of times the trajectory encircles the origin in anticlockwise direction and reflects the cumulative phase evolution of the system:

$$w = \frac{1}{2\pi}\sum_{i=1}^{N}\delta\phi_i \tag{12}$$

where w is the winding number, i is counts the points along the closed loop in the complex ρ-plane, and N is the total number of points. All phase changes are taken in radians; $\delta\phi_i = \arg(\rho_{i+1}) - \arg(\rho_i)$ is the incremental phase change between neighboring points in the trajectory.

In the context of strong coupling, w counts the number of full 2π phase rotations in the complex plane: $w = 1$ corresponds to a single 2π rotation (weak or intermediate coupling), whereas $w = 2$ indicates two full rotations (total 4π phase change), consistent with the presence of two resonant contributions such as polariton branches in the strong coupling regime.

The geometry of ρ-loop also provides insight into damping and coherence in the system. A near-circular, symmetric loop suggests balanced mode line-widths and high coherence. Stretched and/or distorted loops reflect mismatched quality factors ($\gamma_{\text{ex}} \neq \gamma_0$), while noisy or self-intersecting paths may indicate lossy or incoherent coupling. Surface roughness, scattering, and inhomogeneous broadening also appear as distortions in ρ trajectories. These features are often masked in $\Psi(E)$ and $\Delta(E)$ plots. This makes the ρ trajectory a powerful diagnostic tool for evaluating optical coherence and identifying artifacts.

Typical ρ trajectories for a NiPc film measured at $\theta = 70°$ are compared with those obtained over the full θ range (45–80°) in both VASE and VA TIRE modes, as summarized in Table IV. The film with $d = 49.7$ nm ($c = 10$ mg/mL) is shown as a representative example for the thickness range 42.3–63.8 nm ($c = 10$ mg/mL). The dataset, covering the entire angular range as well as the full range of film thicknesses, is provided in the supplementary material, Sec. IM.

At a single $\theta = 70°$, the SE and TIRE ρ trajectories look similar in shape but key differences in scale, offset from the origin (0,0), and symmetry reveal important distinctions in the underlying light–matter interaction.

In SE mode the trajectory forms two large overlapping clockwise loops shifted significantly to the left along $\text{Re}(\rho)$ (Table IV, top left). From Eq. (11), the magnitude of ρ is defined as:

$$|\rho| = \frac{|r_p|}{|r_s|} = \tan\Psi \tag{13}$$

This magnitude determines how far the loop located from the origin in a ρ-trajectory plot:

- $|\rho| = 1$ ($|r_p| \approx |r_s|$): the loop is centered near the origin.
- $|\rho| > 1$ ($|r_p| > |r_s|$): the loop is shifted to the right.
- $|\rho| < 1$ ($|r_p| < |r_s|$): the loop is shifted to the left.

Therefore, the horizontal offset reflects the average ratio of p/s polarized reflectivity. When this ratio is large due to the substrate and/or film geometry, the offset is a background effect rather than a signature of resonance (as evidenced in SE mode ρ trajectory).

TIRE anticlockwise loops (Table IV, bottom left) are more compact and circular, closer to the origin. This reduced offset and increased symmetry imply that the resonance plays a larger role relative to the baseline reflectivity. The TIRE geometry provides stronger vertical field confinement and greater overlap with the excitonic layer, making resonance effects more prominent. This behavior is

TABLE IV. ρ trajectories of NiPc films on gold ($d = 49.7 \pm 3.6$ nm) at fixed angle ($\theta = 70°$) and variable angles ($\theta = 45{-}80°$) in VASE and VA TIRE modes. The photon energy is in the range 0.7–3.5 eV for all measurements. Asterisks (*) indicate the starting points and arrows show the direction of ρ-trajectory evolution.

$\theta = 70°$, SE	$\theta = 45 - 80°$, VASE
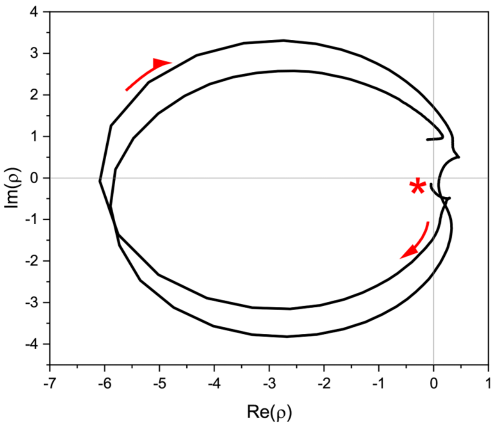	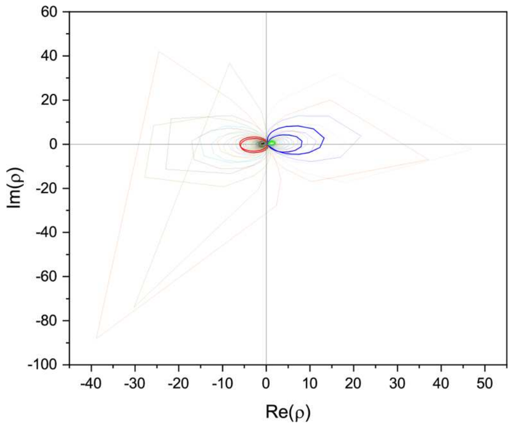
$\theta = 70°$, TIRE	$\theta = 45 - 80°$, VA TIRE
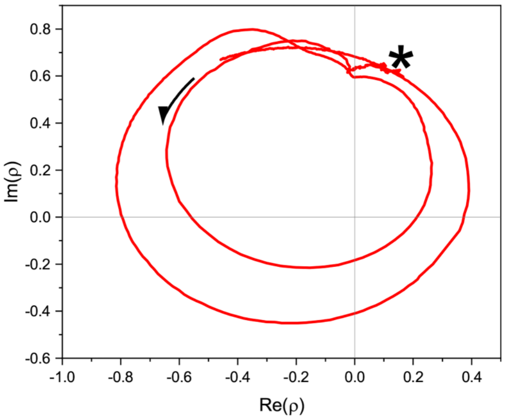	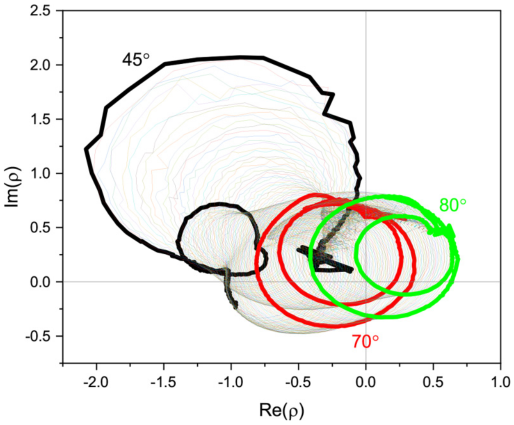

more consistent with conditions favoring stronger exciton–plexciton coupling.

As the θ is varied from 45° to 80°, the VASE mode loops develop into a "butterfly" shape, with two distinct "wings" on opposite sides of the Re(ρ) axis. Each "wing" corresponds to a different side of the phase singularity, where the real part of ρ changes sign. At lower θ, the loop tilts so that the right-hand "wing" dominates (positive Re(ρ)), while at higher θ the tilt reverses and the left-hand "wing" dominates (negative Re(ρ)). This flip in orientation occurs because the relative phase shift between p- and s-polarized light changes with incidence angle, altering the sign of Re(ρ). Despite this angular evolution, the loops remain discrete. They do not merge into a single, smoothly evolving path.

Multi-angle VA TIRE ρ trajectories show distortions and bending in the loop as the angle varies: features that reflect underlying mode splitting and plexciton formation. This is attributed to enhanced vertical field confinement and stronger exciton–plexciton overlap in the TIRE geometry.[65] As strong coupling is usually identified by three linked signatures:[45,66]

(1) Angle-dependent mode splitting (avoided crossing) in Ψ/Δ or reflectance;
(2) Continuous, angle-progressive deformation of the ρ trajectory into elongated "worm" patterns;
(3) Correlated movement of the loop center with θ as polaritonic modes shift in energy.

However, none of these are observed in the VASE data here: there is no avoided crossing, no worm-like chaining, and the loop center remains fixed off-origin. Although the film thickness and molecular concentration are identical, the measurement configuration alone determines whether strong coupling can be observed. Taken together, and contrasted with VA TIRE measurements, which do produce "worm"-like trajectories, these observations indicate that

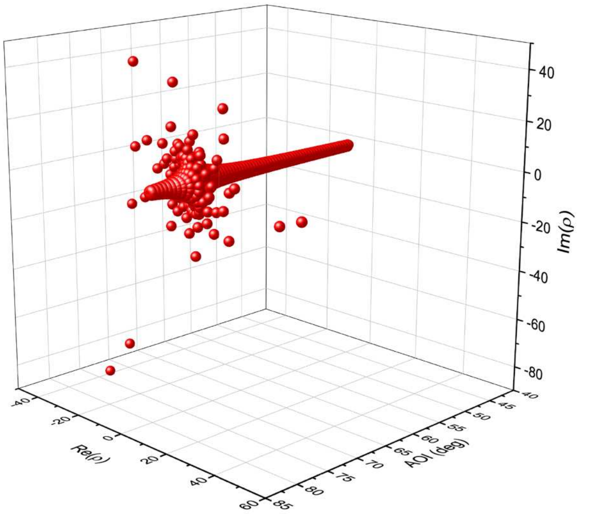

(a) VASE

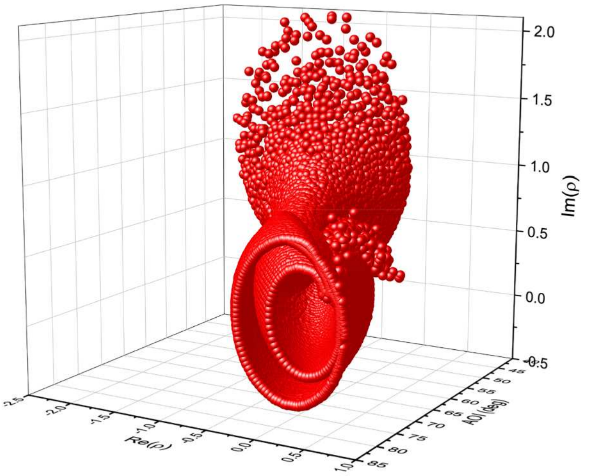

(b) VA TIRE

FIG. 4. Comparison of 3D ρ trajectories measured in (a) VASE and (b) VA TIRE modes. In both cases, the angle of incidence is fixed at $\theta = 70^\circ$, and the photon energy is in the range of 0.7–3.5 eV. The VA TIRE trajectory shows the characteristic multi-loop phase structure associated with strong coupling; the VASE trajectory remains nearly planar.

the VASE response is dominated by interference/absorption features on a strong baseline rather than by coherent exciton–plexciton hybridization.

The difference becomes even more visible in the 3D representations. In VASE mode [Fig. 4(a)], the 3D ρ trajectories forms a long, axis-aligned "tube" with little internal structure, indicating strong reflectance variation but no topological complexity. The TIRE geometry [Fig. 4(b)] reveals a helical structure with twisting and bifurcation in the Re–Im–θ volume. This layered and looping topology is characteristic of strong coupling, where the amplitude and phase of reflected light evolve non-linearly with angle due to hybrid mode formation.

This comparison highlights the limitations of single-angle analysis: spectra recorded at a fixed θ can make systems in fundamentally different coupling regimes appear similar. When ρ trajectories are examined over a sufficiently large range of θ or visualized in 3D, clear distinctions emerge. Notably, only VA TIRE measurements reveal the polaritonic structure of the exciton–plexciton system. VASE data for films of identical thickness and concentration show no angular dispersion, underscoring the importance of measurement geometry and vertical field confinement in accessing the strong coupling regime. These results further demonstrate that 2D or 3D multi-angle ρ-mapping is essential for distinguishing genuine hybridization from interference-related and absorptive features.

G. Winding number

For a representative NiPc film with $d \approx 49.7$ nm, the winding number was calculated to illustrate the typical behavior in this thickness range; the corresponding ρ trajectory encloses the origin twice (Table IV, bottom left) with minimal distortion or noise. This behavior corresponds to a winding number of $w = 2.14$ calculated using Eq. (12), indicating a well-defined, coherent phase evolution and confirming the presence of a topologically protected phase singularity.

A winding number slightly above 2 indicates that the measured phase accumulated a bit more than two full 2π rotations along the trajectory. This excess is usually caused by experimental noise or small deviations from a perfectly closed loop in parameter space. In practice, it means the true winding number is *2*, but the integration picked up a small extra phase contribution from imperfections in the data. Center of the trajectory lies close to the origin (0, 0), enhancing the sensitivity of w to phase changes and increasing the visibility of topological effects.

Figure 5 shows the wrapped and unwrapped phase increments $\delta\phi$ as functions of photon energy. The wrapped quantity is limited to $[-\pi, \pi]$; whenever the true phase increment goes beyond this range, it is shifted by $\pm 2\pi$, creating apparent jumps. Unwrapping removes this 2π periodicity and gives a smooth, continuous phase that directly follows the rotation of complex vector ρ. The total phase shift across the energy interval corresponds to a cumulative rotation of ca. 4π, consistent with the winding number $w \approx 2.14$. This confirms that the trajectory encircles the origin slightly more than twice, with the small excess arising from experimental noise and numerical integration. The steepest phase evolution occurs near the resonance energy, where exciton–plexciton mixing is strongest.

The winding number provides a simple numerical measure of the total phase change, but it reduces all spectral behavior to a single value. By plotting $\arg(\rho)$ against energy (Fig. 5), the complete phase evolution can be seen: showing where phase jumps occur, their size, and how they relate to spectral resonances. Such plots also make phase wrapping (e.g., from $-\pi$ to $+\pi$) easy to

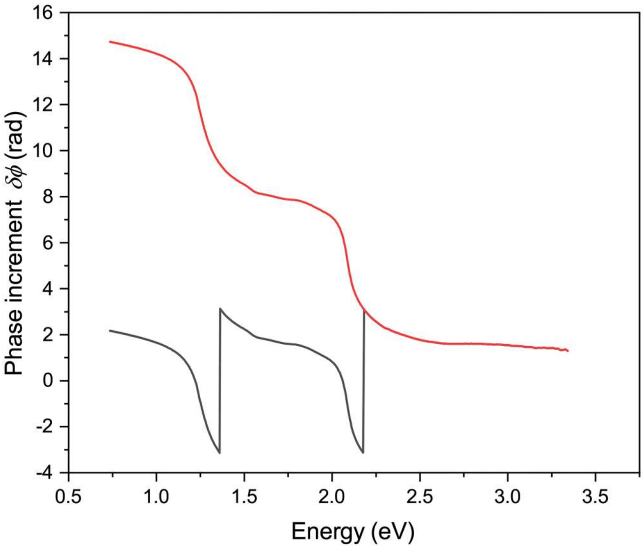

FIG. 5. Wrapped (black) and unwrapped (red) phase increment $\delta\phi(E)$ for the ρ-trajectory of the NiPc film (≈ 50 nm) measured in the TIRE mode at $\theta = 70°$.

identify and help separate the individual contributions that build up to w. However, winding numbers should be interpreted alongside dispersion data to avoid overestimating coupling effects.

IV. CONCLUSIONS

Spectroscopic ellipsometry enabled a detailed investigation of light–matter strong coupling in NiPc thin films on gold substrates. VA TIRE measurements were particularly effective for directly observing polariton band splitting in the Ψ and Δ dispersion maps, with the effect strongly dependent on film thickness.

Films with the thicknesses in the ranges of $d \approx 42-64$ nm showed strong exciton–plexciton coupling. Both, thinner (10 nm) and thicker (252 nm) films exhibited very small splitting. Rabi energies extracted from VA TIRE varied between 0.37 and 0.51 eV, depending on film thickness. Hopfield coefficient analysis vs angle of incidence further revealed the evolution of excitonic and plasmonic fractions in the hybrid modes.

Phase singularities appeared when Ψ was approaching zero, and they were still observed in the strong coupling regime. Their presence was confirmed by closed loops in multi-angle and 3D ρ trajectory plots, serving as topological signatures of hybrid mode formation.

Although VASE showed no clear angular dispersion or direct signatures of strong coupling, it provided essential checks on sample quality and uniformity, detection of weak resonances, and verification that VA TIRE features were not artifacts of inaccurate optical constants or instrumental misalignment.

SUPPLEMENTARY MATERIAL

See the supplementary material for details of the materials used, the structural formula of NiPc, estimation of the light spot size at the sample surface, and analysis of NiPc absorption spectra. Additional sections include determination of the optical parameters of NiPc and extended ellipsometric spectra (VASE and VA TIRE modes) for NiPc films on glass and gold with varying thicknesses and concentrations. It also contains three-dimensional and variable-angle ρ-trajectory data along with further analyses (not included in the main text for clarity).

ACKNOWLEDGMENTS

A.L. gratefully acknowledge funding for this work from the Department of Engineering and Mathematics, Sheffield Hallam University. J.L. and A.C. thank the Université de Rouen Normandie, Département Mesures Physiques for sponsoring and coordinating the Erasmus+ program Student Mobility for Placement, Grant Nos. 68531 (A.C.) and 65418 (J.L.). N.L. thanks Department of Engineering and Mathematics, Sheffield Hallam University and Tapton School for organizing the work experience placement.

AUTHOR DECLARATIONS

Conflict of Interest

The authors have no conflicts to disclose.

Author Contributions

A. Lishchuk: Conceptualization (equal); Data curation (equal); Formal analysis (equal); Funding acquisition (equal); Investigation (lead); Methodology (equal); Project administration (equal); Resources (equal); Software (equal); Supervision (equal); Validation (equal); Visualization (equal); Writing – original draft (equal); Writing – review & editing (equal). **J. Lebourg:** Conceptualization (supporting); Data curation (supporting); Formal analysis (supporting); Funding acquisition (supporting); Investigation (equal); Methodology (supporting); Project administration (supporting); Resources (equal); Software (equal); Supervision (supporting); Validation (equal); Visualization (equal); Writing – original draft (supporting); Writing – review & editing (supporting). **N. Lishchuk:** Conceptualization (supporting); Data curation (supporting); Formal analysis (equal); Funding acquisition (supporting); Investigation (equal); Methodology (supporting); Project administration (supporting); Resources (supporting); Software (equal); Supervision (supporting); Validation (supporting); Visualization (equal); Writing – original draft (supporting); Writing – review & editing (equal). **A. Campanella:** Conceptualization (equal); Data curation (equal); Formal analysis (equal); Funding acquisition (equal); Investigation (equal); Methodology (equal); Project administration (equal); Resources (equal); Software (equal); Supervision (equal); Validation (equal); Visualization (equal); Writing – original draft (equal); Writing – review & editing (equal). **H. Arwin:** Conceptualization (equal); Data curation (equal); Formal analysis (equal); Funding acquisition (supporting); Investigation (equal); Methodology (equal); Project administration (supporting); Resources (equal); Software (equal); Supervision (supporting); Validation (equal); Visualization (equal); Writing – original draft (equal); Writing – review & editing (lead). **A. Nabok:** Conceptualization (equal); Data curation (equal);

Formal analysis (equal); Funding acquisition (equal); Investigation (equal); Methodology (equal); Project administration (equal); Resources (equal); Software (equal); Supervision (equal); Validation (equal); Visualization (equal); Writing – original draft (equal); Writing – review & editing (equal).

DATA AVAILABILITY

The data that support the findings of this study are available within the article and its supplementary material.

REFERENCES

[1] T. W. Ebbesen, "Hybrid light–matter states in a molecular and material science perspective," Acc. Chem. Res. **49**, 2403–2412 (2016).

[2] P. Törmä and W. L. Barnes, "Strong coupling between surface plasmon polaritons and emitters: A review," Rep. Prog. Phys. **78**, 013901 (2014).

[3] L. Novotny, "Strong coupling, energy splitting, and level crossings: A classical perspective," Am. J. Phys. **78**, 1199–1202 (2010).

[4] D. S. Dovzhenko, S. V. Ryabchuk, Y. P. Rakovich, and I. R. Nabiev, "Light–matter interaction in the strong coupling regime: Configurations, conditions, and applications," Nanoscale **10**, 3589–3605 (2018).

[5] W. Wang, P. Vasa, R. Pomraenke, R. Vogelgesang, A. De Sio, E. Sommer, M. Maiuri, C. Manzoni, G. Cerullo, and C. Lienau, "Interplay between strong coupling and radiative damping of excitons and surface plasmon polaritons in hybrid nanostructures," ACS Nano **8**, 1056–1064 (2014).

[6] M. Hertzog, M. Wang, J. Mony, and K. Börjesson, "Strong light–matter interactions: A new direction within chemistry," Chem. Soc. Rev. **48**, 937–961 (2019).

[7] A. P. Manuel, A. Kirkey, N. Mahdi, and K. Shankar, "Plexcitonics—Fundamental principles and optoelectronic applications," J. Mater. Chem. C **7**, 1821–1853 (2019).

[8] M. Sukharev and A. Nitzan, "Optics of exciton-plasmon nanomaterials," J. Phys.: Condens. Matter. **29**, 443003 (2017).

[9] N. Ismail, C. C. Kores, D. Geskus, and M. Pollnau, "Fabry-Pérot resonator: Spectral line shapes, generic and related airy distributions, linewidths, finesses, and performance at low or frequency-dependent reflectivity," Opt. Express **24**, 16366 (2016).

[10] S. Guldin, M. Kolle, M. Stefik, R. Langford, D. Eder, U. Wiesner, and U. Steiner, "Tunable mesoporous bragg reflectors based on block-copolymer self-assembly," Adv. Mater. **23**, 3664–3668 (2011).

[11] D. Farnesi, S. Pelli, S. Soria, G. Nunzi Conti, X. Le Roux, M. Montesinos Ballester, L. Vivien, P. Cheben, and C. Alonso-Ramos, "Metamaterial engineered silicon photonic coupler for whispering gallery mode microsphere and disk resonators," Optica **8**, 1511 (2021).

[12] D. Englund, I. Fushman, and J. Vuckovic, "General recipe for designing photonic crystal cavities," Opt. Express **13**, 5961 (2005).

[13] Y. Zhang, T. Zhou, B. Han, A. Zhang, and Y. Zhao, "Optical bio-chemical sensors based on whispering gallery mode resonators," Nanoscale **10**, 13832–13856 (2018).

[14] N. A. Toropov, G. Cabello, M. P. Serrano, R. R. Gutha, M. Rafti, and F. Vollmer, "Review of biosensing with whispering-gallery mode lasers," Light-Sci. Appl. **10**, 42 (2021).

[15] I. Plikusienė, E. Bužavaitė-Vertelienė, V. Mačiulis, A. Valavičius, A. Ramanavičienė, and Z. Balevičius, "Application of Tamm plasmon polaritons and cavity modes for biosensing in the combined spectroscopic ellipsometry and quartz crystal microbalance method," Biosensors **11**, 501 (2021).

[16] P. A. Thomas, K. S. Menghrajani, and W. L. Barnes, "Cavity-free ultrastrong light-matter coupling," J. Phys. Chem. Lett. **12**, 6914–6918 (2021).

[17] K. S. Menghrajani, A. B. Vasista, W. J. Tan, and W. L. Barnes, "Molecular strong coupling: An exploration employing open, half- and full planar cavities," arXiv:2211.08300 (2022).

[18] K. S. Menghrajani, A. B. Vasista, W. J. Tan, P. A. Thomas, F. Herrera, and W. L. Barnes, "Molecular strong coupling and cavity finesse," J. Phys. Chem. Lett. **15**, 7449–7457 (2024).

[19] A. B. P. Lever, *Advances in Inorganic Chemistry and Radiochemistry, Vol. 7: Phthalocyanines* (Academic Press, 1990).

[20] J. Mack and M. J. Stillman, "Assignment of the optical spectra of metal phthalocyanines through spectral band deconvolution analysis and ZINDO calculations," Coord. Chem. Rev. **219-221**, 993–1032 (2001).

[21] M.-S. Liao and S. Scheiner, "Electronic structure and bonding in metal phthalocyanines, metal = Fe, Co, Ni, Cu, Zn, Mg," J. Chem. Phys. **114**, 9780–9791 (2001).

[22] R. R. Cranston and B. H. Lessard, "Metal phthalocyanines: Thin-film formation, microstructure, and physical properties," RSC Adv. **11**(35), 21716–21737 (2021).

[23] PubChem, see https://pubchem.ncbi.nlm.nih.gov/compound/6528991 for "Pubchem compound summary for CID-6528991" (2025).

[24] G. Zengin, G. Johansson, P. Johansson, T. J. Antosiewicz, M. Käll, and T. Shegai, "Approaching the strong coupling limit in single plasmonic nanorods interacting with J-aggregates," Sci. Rep. **3**, 3074 (2013).

[25] Z. He, F. Li, P. Zuo, C. Xu, W. He, J. He, Y. Zhou, Q. Zhang, K. Chen, H. Huang, and L. Hu, "Strong coupling in a hybrid system of silver nanoparticles and J-aggregates at room temperature," J. Phys. Chem. C **126**, 17141–17151 (2022).

[26] X. Bi, Z. Li, C. Zhang, Q. You, Y. Li, Y. Wang, and P. Wang, "Strong coupling of Ag@Au hollow nanocube/J-aggregate heterostructures by absorption spectra," J. Phys. Chem. C **126**, 10566–10573 (2022).

[27] K. Tani, C. Ito, Y. Hanawa, M. Uchida, K. Otaguro, H. Horiuchi, and H. Hiratsuka, "Photophysical property and photostability of J-aggregate thin films of thiacyanine dyes prepared by the spin-coating method," J. Phys. Chem. B **112**, 836–844 (2008).

[28] F. Wurthner, T. E. Kaiser, and C. R. Saha-Möller, "J-aggregates: From serendipitous discovery to supramolecular engineering of functional dye materials," Angew. Chem. Int. Ed. **50**, 3376–3410 (2011).

[29] A. J. Musser and J. Clark, "Triplet-pair states in organic semiconductors," Annu. Rev. Phys. Chem. **70**, 323–351 (2019).

[30] M. Litinskaya and P. Reineker, "Loss of coherence of exciton polaritons in inhomogeneous organic microcavities," Phys. Rev. B **74**, 165320 (2006).

[31] A. Wang, J. Ye, M. G. Humphrey, and C. Zhang, "Graphene and carbon-nanotube nanohybrids covalently functionalized by porphyrins and phthalocyanines for optoelectronic properties," Adv. Mater. **30**, 1705704 (2018).

[32] H. Raether, *Surface Plasmons on Smooth and Rough Surfaces and on Gratings*, Springer Tracts in Modern Physics Vol. 111 (Springer, Berlin, 1988).

[33] V. Amendola, R. Pilot, M. Frasconi, O. M. Maragò, and M. A. Iatì, "Surface plasmon resonance in gold nanoparticles: A review," J. Phys.: Condens. Matter **29**, 203002 (2017).

[34] A. Mendoza-Galván, K. Järrendahl, A. Dmitriev, T. Pakizeh, M. Käll, and H. Arwin, "Optical response of supported gold nanodisks," Opt. Express **19**, 12093 (2011).

[35] A. G. Al-Rubaye, A. Nabok, and A. Tsargorodska, "Spectroscopic ellipsometry study of gold nanostructures for LSPR bio-sensing applications," Sens. Bio-Sens. Res. **12**, 30–35 (2017).

[36] Y.-M. Lee, H. Choi, S.-E. Kim, J. Kim, H. W. Kim, and J.-E. Park, "Plasmon–exciton strong coupling in colloidal au nanocubes with layered molecular J-aggregates," Nano Lett. **24**, 16115–16123 (2024).

[37] A. Lishchuk, G. Kodali, J. A. Mancini, M. Broadbent, B. Darroch, O. A. Mass, A. Nabok, P. L. Dutton, C. N. Hunter, P. Törmä, and G. J. Leggett, "A synthetic biological quantum optical system," Nanoscale **10**, 13064–13073 (2018).

[38] *Ellipsometry in the Measurement of Surfaces and Thin Films*, edited by E. Passaglia, R. R. Stromberg, and J. Kruger (Miscellaneous Publication, U.S. National Bureau of Standards, Washington, DC, 1964), Vol. 256.

[39] H. Arwin, M. Poksinski, and K. Johansen, "Total internal reflection ellipsometry: Principles and applications," Appl. Opt. **43**, 3028–3036 (2004).

[40] S. Pirotta, M. Patrini, M. Liscidini, M. Galli, G. Dacarro, G. Canazza, G. Guizzetti, D. Comoretto, and D. Bajoni, "Strong coupling between excitons in

organic semiconductors and bloch surface waves," Appl. Phys. Lett. **104**, 051111 (2014).

[41] T. W. H. Oates, H. Wormeester, and H. Arwin, "Characterization of plasmonic effects in thin films and metamaterials using spectroscopic ellipsometry," Prog. Surf. Sci. **86**, 328–376 (2011).

[42] H. Hilmer, C. Sturm, R. Schmidt-Grund, B. Rheinländer, and M. Grundmann, "Observation of strong light-matter coupling by spectroscopic ellipsometry," Superlattices Microstruct. **47**, 19–23 (2010).

[43] Z. Balevičius, "Strong coupling between Tamm and surface plasmons for advanced optical bio-sensing," Coatings **10**, 1187 (2020).

[44] E. Bužavaitė-Vertelienė, V. Vertelis, and Z. Balevičius, "The experimental evidence of a strong coupling regime in the hybrid tamm plasmon-surface plasmon polariton mode," Nanophotonics **10**, 1565–1571 (2021).

[45] P. A. Thomas, W. J. Tan, H. A. Fernandez, and W. L. Barnes, "A new signature for strong light–matter coupling using spectroscopic ellipsometry," Nano Lett. **20**, 6412–6419 (2020).

[46] A. I. Aristov, U. Zywietz, A. B. Evlyukhin, C. Reinhardt, B. N. Chichkov, and A. V. Kabashin, "Laser-ablative engineering of phase singularities in plasmonic metamaterial arrays for biosensing applications," Appl. Phys. Lett. **104**, 071101 (2014).

[47] G. Ermolaev, K. Voronin, D. G. Baranov, V. Kravets, G. Tselikov, Y. Stebunov, D. Yakubovsky, S. Novikov, A. Vyshnevyy, A. Mazitov, I. Kruglov, S. Zhukov, R. Romanov, A. M. Markeev, A. Arsenin, K. S. Novoselov, A. N. Grigorenko, and V. Volkov, "Topological phase singularities in atomically thin high-refractive-index materials," Nat. Commun. **13**, 2049 (2022).

[48] R. S. Jassas, A. Timoumi, S. N. Alamri, M. Alamri, H. M. Altass, Y. Raviprakash, A. Abd-El-Aziz, O. O. Alameer, Z. Moussa, N. Ma, and S. A. Ahmed, "Insights into the physical characteristics of spin coating films of organometallic materials based on phthalocyanine with nickel, copper, manganese and silicon," J. Inorg. Organomet. Polym. Mater. **34**, 3068–3075 (2024).

[49] Q. Zhou, Z.-F. Liu, T. J. Marks, and P. Darancet, "Electronic structure of metallophthalocyanines, MPc (M = Fe, Co, Ni, Cu, Zn, Mg) and fluorinated MPc," J. Phys. Chem. A **125**, 4055–4061 (2021).

[50] P. Day and R. J. P. Williams, "Spectra and photo conduction of phthalocyanine complexes (I)," J. Chem. Phys. **37**, 567–570 (1962).

[51] T. Wakamatsu and K. Aizawa, "Penetration-depth characteristics of evanescent fields at metal attenuated total reflection," Jpn. J. Appl. Phys. **44**, 4272–4274 (2005).

[52] V. M. Agranovich and Y. N. Gartstein, "Spatial dispersion and negative refraction of hybrid polaritons in nanostructured media," Phys.-Usp. **49**, 1029–1044 (2006).

[53] J. Bellessa, C. Symonds, K. Vynck, A. Lemaitre, A. Brioude, L. Beaur, J. C. Plenet, P. Viste, D. Felbacq, E. Cambril, and P. Valvin, "Giant rabi splitting between localized mixed plasmon-exciton states in a two-dimensional array of nanosize metallic disks in an organic semiconductor," Phys. Rev. B **80**, 033303 (2009).

[54] T. K. Hakala, J. J. Toppari, A. Kuzyk, M. Pettersson, H. Tikkanen, H. Kunttu, and P. Törmä, "Vacuum rabi splitting and strong-coupling dynamics for surface-plasmon polaritons and rhodamine 6G molecules," Phys. Rev. Lett. **103**, 053602 (2009).

[55] D. G. Lidzey, D. D. C. Bradley, M. S. Skolnick, T. Virgili, S. Walker, and D. M. Whittaker, "Strong exciton–photon coupling in an organic semiconductor microcavity," Nature **395**, 53–55 (1998).

[56] A. Tsargorodska, M. L. Cartron, C. Vasilev, G. Kodali, O. A. Mass, J. J. Baumberg, P. L. Dutton, C. N. Hunter, P. Törmä, and G. J. Leggett, "Strong coupling of localized surface plasmons to excitons in light-harvesting complexes," Nano Lett. **16**, 6850–6856 (2016).

[57] A. W. Kanzler, H. Sun, and K. F. Freed, "Dipole moments, transition moments, oscillator strengths, radiative lifetimes, and overtone intensities for CH and CH^+ as computed by quasi-degenerate many-body perturbation theory," Int. J. Quantum Chem. **39**, 269–286 (1991).

[58] S. Kéna-Cohen and S. R. Forrest, "Room-temperature polariton lasing in an organic single-crystal microcavity," Nat. Photonics **4**, 371–375 (2010).

[59] J. J. Hopfield, "Theory of the contribution of excitons to the complex dielectric constant of crystals," Phys. Rev. **112**, 1555–1567 (1958).

[60] Sigma-Aldrich, "Nickel (II) 1,4,8,11,15,18,22,25-octabutoxy-29h,31h-phthalocyanine," https://www.sigmaaldrich.com/GB/en/product/aldrich/360635.

[61] R. C. Hilborn, "Einstein coefficients, cross sections, f values, dipole moments, and all that," arXiv:physics/0202029 [physics.atom-ph] (2002).

[62] J. Anulytė, "Strongly coupled extended plasmonic states for coherent energy exchange," (2025).

[63] H. G. Tompkins and W. A. Mcgahan, *Spectroscopic Ellipsometry and Reflectometry: A User's Guide* (John Wiley & Sons, Cop, 1999).

[64] G. Simone, "Demonstrating more than 2π phase modulation in non-Hermitian asymmetric multilayers," New J. Phys. **25**(12), 123027 (2023).

[65] N. Zorn Morales, D. S. Rühl, S. Sadofev, G. Ligorio, E. List-Kratochvil, G. Kewes, and S. Blumstengel, "Strong coupling of monolayer WS_2 excitons and surface plasmon polaritons in a planar Ag/WS_2 hybrid structure," Phys. Rev. B **108**, 165426 (2023).

[66] G. Carini, R. Niemann, N. S. Mueller, M. Wolf, and A. Paarmann, "Surface phonon polariton ellipsometry," ACS Photonics **12**, 792–800 (2025).